

Thermoelectric performance of XI_2 (X = Ge, Sn, Pb) bilayers

Nan Lu(陆楠) and Jie Guan(管杰)

Citation: Chin. Phys. B, 2022, 31 (**4**): 047201. DOI: 10.1088/1674-1056/ac474c
Journal homepage: http://cpb.iphy.ac.cn; http://iopscience.iop.org/cpb

What follows is a list of articles you may be interested in

Effect of carbon nanotubes addition on thermoelectric properties of $Ca_3Co_4O_9$ ceramics

Ya-Nan Li(李亚男), Ping Wu(吴平), Shi-Ping Zhang(张师平), Yi-Li Pei(裴艺丽), Jin-Guang Yang(杨金光), Sen Chen(陈森), and Li Wang(王立)

Chin. Phys. B, 2022, 31 (**4**): 047203. DOI: 10.1088/1674-1056/ac4bd2

Significant role of nanoscale Bi-rich phase in optimizing thermoelectric performance of Mg_3Sb_2

Yang Wang(王杨), Xin Zhang(张忻), Yan-Qin Liu(刘燕琴), Jiu-Xing Zhang(张久兴), Ming Yue(岳明)

Chin. Phys. B, 2020, 29 (**6**): 067201. DOI: 10.1088/1674-1056/ab84cd

Thermoelectric properties of lower concentration K-doped $Ca_3Co_4O_9$ ceramics

Ya-Nan Li(李亚男), Ping Wu(吴平), Shi-Ping Zhang(张师平), Sen Chen(陈森), Dan Yan(闫丹), Jin-GuangYang(杨金光), Li Wang(王立), Xiu-Lan Huai(淮秀兰)

Chin. Phys. B, 2018, 27 (**5**): 057201. DOI: 10.1088/1674-1056/27/5/057201

An overview of thermoelectric films: Fabrication techniques, classification, and regulation methods

Jing-jing Feng(冯静静), Wei Zhu(祝薇), Yuan Deng(邓元)

Chin. Phys. B, 2018, 27 (**4**): 047210. DOI: 10.1088/1674-1056/27/4/047210

Effect of Nb doping on microstructures and thermoelectric properties of $SrTiO_3$ ceramics

Da-Quan Liu(刘达权), Yu-Wei Zhang(张玉伟), Hui-Jun Kang(康慧君), Jin-Ling Li(李金玲), Xiong Yang(杨雄), Tong-Min Wang(王同敏)

Chin. Phys. B, 2018, 27 (**4**): 047205. DOI: 10.1088/1674-1056/27/4/047205

Thermoelectric performance of XI_2 (X = Ge, Sn, Pb) bilayers

Nan Lu(陆楠) and Jie Guan(管杰)†

School of Physics, Southeast University, Nanjing 211189, *China*

(Received 14 September 2021; revised manuscript received 16 November 2021; accepted manuscript online 31 December 2021)

We study the thermal and electronic transport properties as well as the thermoelectric (TE) performance of three two-dimensional (2D) XI_2 (X = Ge, Sn, Pb) bilayers using density functional theory and Boltzmann transport theory. We compared the lattice thermal conductivity, electrical conductivity, Seebeck coefficient, and dimensionless figure of merit (ZT) for the XI_2 monolayers and bilayers. Our results show that the lattice thermal conductivity at room temperature for the bilayers is as low as $\sim$ 1.1 W·m^{-1}·K^{-1}–1.7 W·m^{-1}·K^{-1}, which is about 1.6 times as large as the monolayers for all the three materials. Electronic structure calculations show that all the XI_2 bilayers are indirect-gap semiconductors with the band gap values between 1.84 eV and 1.96 eV at PBE level, which is similar as the corresponding monolayers. The calculated results of ZT show that the bilayer structures display much less direction-dependent TE efficiency and have much larger n-type ZT values compared with the monolayers. The dramatic difference between the monolayer and bilayer indicates that the inter-layer interaction plays an important role in the TE performance of XI_2, which provides the tunability on their TE characteristics.

Keywords: 2D group-IV diiodide, thermoelectric materials, bilayers

PACS: 72.15.Eb, 72.15.Jf, 72.20.–i, 73.63.–b **DOI:** 10.1088/1674-1056/ac474c

1. Introduction

High quality thermoelectric (TE) materials and their applications have provided an effective way for the transforming from heat to electricity and received intense researches for the significant contributions to the global sustainable energy solution.[1–4] Traditionally, the efficiency of TE materials is measured primarily by the dimensionless figure of merit, ZT, defined as[1,5] $ZT = S^2\sigma T/(\kappa_L + \kappa_e)$, where S, σ, T, κ_L, κ_e are the Seebeck coefficient, electrical conductivity, absolute temperature, lattice thermal conductivity, and electrical thermal conductivity, respectively. In terms of the formula of ZT, high Seebeck coefficient, high electrical conductivity, and low thermal conductivity are required to enhance the TE performance.

Conventionally, increasing the electrical power factor ($PF = S^2\sigma$) and reducing the κ_L are two general approaches to obtain high-quality TE materials. Regarding increasing the PF, one successful way is to get a large density of states (DOS) effective mass by converging the valence (or conduction) bands.[6] Various strategies such as alloying,[7] elemental doping,[8] and strain engineering[9,10] have been developed to achieve the convergence of the bands and consequently to improve the TE performance. For the reduction of κ_L, it is an effective strategy to enhance the phonon scattering by introducing multiscale scattering centers, *e.g.*, point-defects[11,12] or grain boundaries.[13] However, suppressing κ_L through the phonon engineering is actually difficult to achieve without simultaneously affecting electron transport.[6] Hence, seeking new materials with intrinsically high power factor and low thermal conductivity is a preferable approach to obtain high TE performance.

In 1993, the seminal work of Hicks and Dresselhaus showed that reducing the dimension of the system could significantly increase ZT value, due to the enhanced PF caused by an increased DOS near the Fermi level and the reduced κ_L caused by the increased phonon scattering from the surface.[2,14] With the emerging field of layered materials in the past decades, a number of investigations have been conducted on two-dimensional (2D) TE materials, such as SnSe,[15] SnTe,[16] GeTe,[17] SiTe,[18] XSb (X = Si, Ge, Sn),[19] phosphorene,[20,21] and transition metal dichalcogenides (TMDs).[22–24] Recently, the 2D group-IV diiodide family, including PbI_2, GeI_2, SnI_2, and SiI_2, have shown excellent thermoelectric performance.[25–27] Theoretical results showed that the maximum ZT value is 4.04 at 600 K for GeI_2 monolayer[26] and is 4.9 at 900 K for PbI_2 monolayer,[25] which are better than the well-known TMDs and other 2D materials. On the other hand, it is well known that the physical properties of 2D materials are sensitive to inter-layer interaction[28] and in experiment, it is not easy to obtain the monolayer for most 2D materials. Thus, it is intriguing to explore the TE performance for the multilayers of 2D group-IV diiodides.

In this work, by combining *ab initio* density functional theory (DFT) with the Boltzmann transport theory, we compared the electrical and thermal transport properties between the monolayers and bilayers of 2D XI_2 (X = Ge, Sn, Pb). Phonon spectra have been calculated to confirm the dynamical stability of all the 2D XI_2 structures. The κ_L, group velocity (V_g), and phonon lifetime (τ_{ph}) were calculated and the re-

†Corresponding author. E-mail: guanjie@seu.edu.cn

© 2022 Chinese Physical Society and IOP Publishing Ltd

sults show that the κ_L at room temperature for the bilayers are about 1.6 times as large as the corresponding monolayers for all the three materials, which is possibly caused by the larger τ_{ph} for bilayer. Both acoustic and optic phonon modes contribute to the thermal conductivity as a result of the relatively low frequency of the optical phonon modes. Electronic structure was investigated and all the monolayer and bilayer structures are shown to be semiconducting with an indirect band gap close to 2 eV. Carrier mobility (μ) and relaxation time (τ) were also calculated to further explore the electrical transport properties. Finally, the values of the S, σ, PF, and ZT along different directions were compared between the monolayers and bilayers of XI_2. The results show that for all the three XI_2 structures, the bilayers display much less direction-dependent TE efficiency and have much larger n-type ZT values compared with the monolayers. The dramatic difference between the monolayer and bilayer indicates that the inter-layer interaction plays an important role in the TE performance of XI_2, which provides an effective tunability on their TE characteristics.

2. Theoretical method

The lattice thermal transport properties can be calculated based on the phonon Boltzmann transport equation (BTE) and the interatomic force constant (IFC) obtained from DFT calculations. The lattice thermal conductivity along α direction is defined as[29]

$$\kappa_L^{\alpha\alpha} = \frac{1}{k_B T^2 NV} \sum_{q,\nu} n_{q\nu}(n_{q\nu}+1)(\hbar\omega_{q\nu})^2 v_{q\nu}^{\alpha} F_{q\nu}^{\alpha}, \tag{1}$$

where k_B, T, N, and V are the Boltzmann constant, the absolutely temperature, the total number of q points in the first Brillouin zone, and the unit cell volume, respectively. $n_{q\nu}$, $\omega_{q\nu}$, and $v_{q\nu}^{\alpha}$ are equilibrium Bose–Einstein distribution function, phonon frequency, and the phonon group velocity along the α direction of phonon mode $q\nu$. $F_{q\nu}^{\alpha}$ is defined as[29]

$$F_{q\nu}^{\alpha} = (v_{q\nu}^{\alpha} + \Delta_{q\nu})\tau_{q\nu}, \tag{2}$$

where $\tau_{q\nu}$ is the phonon relaxation time of mode $q\nu$. All the calculations are carried out with the DFT method, as implemented in the Vienna *ab initio* simulation package (VASP).[30] We choose the generalized gradient approximation (GGA) in the Perdew–Burke–Ernzerhof (PBE) parametrization for the exchange–correlation functional. To avoid the interactions between adjacent layers, the vacuum region is set in excess of 20 Å. The cutoff energy is set as 500 eV for the plane wave basis. A $9\times9\times1$ k-mesh is used during structural relaxation for the unit cell until the energy differences are converged within 10^{-6} eV, with a Hellman–Feynman force convergence threshold of 10^{-3} eV/Å.

The lattice thermal conductivity is calculated by solving the BTE implemented with a fully iterative self-consistent program in ShengBTE package.[31] When using ShengBTE, the 2nd-order (harmonic) and the 3rd-order (anharmonic) IFCs matrixes are required. The harmonic IFCs are obtained using density functional perturbation theory, which calculates the dynamical matrix through the linear response of electron density.[32] The $5\times5\times1$ supercell with $3\times3\times1$ k-mesh is used to ensure the convergence. The phonon dispersion is obtained using the Phonopy code.[33] Besides the harmonic IFCs mentioned above, the $4\times4\times1$ supercell and $3\times3\times1$ k-mesh are used to obtain the anharmonic IFCs, and an interaction range including the forth-nearest-neighbor atoms is considered. TE properties were computed by solving the BTE under a constant relaxation time τ and a rigid band approximation performed in the BoltztraP2 code.[34] The Seebeck coefficient S and electrical conductivity σ can be obtained by investigating the electronic transport properties based on DFT calculations and the integration of the transport distribution $\Xi(\varepsilon) = \sum_{\boldsymbol{k}} \boldsymbol{v}_{\boldsymbol{k}} \otimes \boldsymbol{v}_{\boldsymbol{k}} \tau_{\boldsymbol{k}}$[35]

$$\sigma(\mu,T) = e^2 \int \Xi(\varepsilon)\left(-\frac{\partial f_0}{\partial \varepsilon}\right) \mathrm{d}\varepsilon, \tag{3}$$

$$S(\mu,T) = \frac{e k_B}{\sigma} \int \Xi(\varepsilon)\left(-\frac{\partial f_0}{\partial \varepsilon}\right) \frac{\varepsilon-\mu}{k_B T} \mathrm{d}\varepsilon, \tag{4}$$

where f_0 is the equilibrium Fermi–Dirac distribution function, k_B is the Boltzmann constant, and μ is the chemical potential. The $\boldsymbol{v}_{\boldsymbol{k}}$ and $\tau_{\boldsymbol{k}}$ are the group velocity and relaxation time at state $\boldsymbol{k}$, respectively. We used a very dense k-point mesh of $60\times60\times1$ to obtain a convergent density of states. The electrical conductivity (σ/τ) we obtained is dependent on the carrier relaxation time τ. The electronic thermal conductivity κ_e is calculated using the Wiedemann–Franz law, $\kappa_e = L\sigma T$, where L is the Lorenz number. Here, we use the Lorenz number of 1.5×10^{-8} W·Ω·K^{-1}.[36]

3. Results and discussion

The equilibrium structures for the monolayers and bilayers of XI_2 are shown in Fig. 1. The monolayers exhibit buckled sandwich hexagonal crystal structure with the space group of 164 (P-3m1). There are one X atom and two I atoms in a unit cell. Our DFT calcultaions show that the lattice constants are 4.30 Å, 4.57 Å, and 4.66 Å for GeI_2, SnI_2, and PbI_2, respectively, which are in good agreement with previous reported values.[37,38] For all the three XI_2 bilayers, AA-stacking is found energetically preferable. The inter-layer distances are respectively 7.75 Å, 7.67 Å, 7.86 Å in GeI_2, SnI_2, and PbI_2. The obtained inter-layer binding energies for all the XI_2 bilayers are less than 0.01 eV/atom at PBE level, which indicates a typical van der Waals (vdW) interaction.

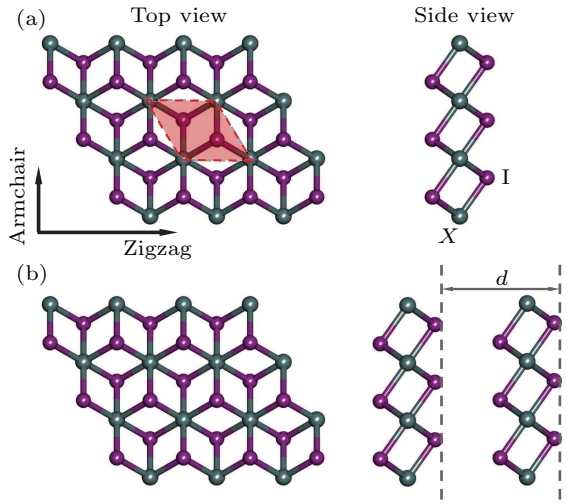


Fig. 1. Ball and stick model for the equilibrium structures of an XI_2 (X = Ge, Sn, Pb) (a) monolayer and (b) bilayer. Both top and side views are shown. The X and I atoms are shown in green and mauve balls, respectively. d is the inter-layer distance in the bilayer. The primitive cell in the top view is denoted by the red shadow.

To examine the dynamical stability of the 2D XI_2 structures, we calculated the phonon dispersion using Phonopy code[32] and have plotted our results in Fig. 2. We find that there are three acoustic modes, including out-of-plane acoustic (ZA) mode, in-plane transverse acoustic (TA) mode, and in-plane longitudinal acoustic (LA) mode, for all the structures and six (fifteen) optical modes for the monolayers (bilayers). We should note that phonon calculations for 2D structures with the unique soft ZA mode are very demanding on precision.[39] We find our phonon spectra to be essentially free of imaginary frequencies associated with decay modes. The tiny imaginary frequencies near the Γ point of the ZA mode ($\omega \lesssim 1\mathrm{i}\ \mathrm{cm}^{-1}$) is an artifact related to numerical precision.[39] The absence of imaginary frequencies in the phonon spectra indicates the dynamical stability of the XI_2 layers. For both of the monolayers and bilayers, the maximum vibration frequencies $\omega_{\max}$ of the three materials gradually shift down with the increasing atomic mass of Ge, Sn, and Pb. Similar to the monatomic linear chain model, the vibration frequency of the phonon mode is dominated by the average atomic mass ($\bar{M}$) and interatomic bonding, and can be qualitatively estimated by $\omega \propto \sqrt{\beta/\bar{M}}$,[40] where β is the force constant. The trend of $\omega_{\max}$ can be understood because the increasing atomic number leads to the increasing interatomic distance and consequently decreasing force constant, as well as the increasing $\bar{M}$ in order of GeI_2, SnI_2, PbI_2. The trend of $\omega_{\max}$ also indicates the similar decrease from GeI_2 to PbI_2 in the lattice thermal conductivity. To confirm this inference, we then explore the κ_L of XI_2 in the next section.

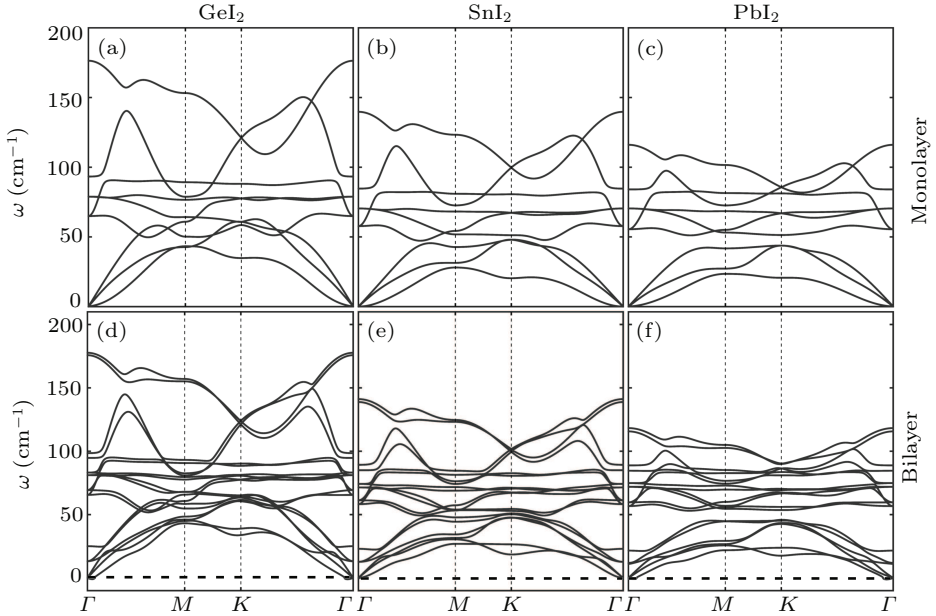


Fig. 2. Phonon dispersion in the first Brillouin zone for the monolayer (upper panel) and bilayer (lower panel) of [(a), (d)] GeI_2, [(b), (e)] SnI_2 and [(c), (f)] PbI_2, respectively.

Based on the phonon Boltzmann transport equation (BTE) and the interatomic force constant (IFC), we calculated the κ_L of the XI_2 structures using the iterative method in ShengBTE code.[31] As the results plotted in Fig. 3, κ_L decreases as temperature increases and the values for the monolayers at 300 K reach 1.14 $\mathrm{W{\cdot}m^{-1}{\cdot}K^{-1}}$, 0.78 $\mathrm{W{\cdot}m^{-1}{\cdot}K^{-1}}$, and 0.63 $\mathrm{W{\cdot}m^{-1}{\cdot}K^{-1}}$ for GeI_2, SnI_2, and PbI_2, respectively. Our results of GeI_2 and PbI_2 are consistent with previously reported theoretical results.[26,41] The values of κ_L for the bilayers (1.74 $\mathrm{W{\cdot}m^{-1}{\cdot}K^{-1}}$, 1.25 $\mathrm{W{\cdot}m^{-1}{\cdot}K^{-1}}$, 1.05 $\mathrm{W{\cdot}m^{-1}{\cdot}K^{-1}}$ for GeI_2, SnI_2, PbI_2 at 300 K, respectively) are about 1.6 times as large as that for the monolayers but still at a relatively low level, which ensures their high TE efficiency. Our results of the low in-plane κ_L for PbI_2 monolayer and bilayer are also reasonably consistent with the experimental results of the crystalline PbI_2 (0.681 $\mathrm{W{\cdot}m^{-1}{\cdot}K^{-1}}$ at 300 K)[42] and the rela-

tively low Debye temperature estimated by the experimentally measured temperature-dependent band gap values.[43] What is more, the values of κ_L are found decreasing in order of the increasing atom mass from Ge to Pb, which is consistent with the phonon dispersion results discussed above.

The group velocity and the phonon lifetime have been calculated to further explore the internal physical mechanism of the intrinsically low κ_L of the XI_2 layers. The V_g of each phonon mode is calculated based on the second-order (harmonic) interatomic force constants. As shown in Figs. 4(a)–4(c), the monolayers and bilayers have similar distributions of V_g for all the XI_2 structures. In general, the V_g decreases with the atomic mass increasing from Ge, Sn to Pb, indicating the decreasing κ_L from GeI_2 to PbI_2. Conventionally, the acoustic modes at the low frequency dominate the thermal conductivity, which is because the optical modes have relatively low group velocities and hard to be excited for their high frequency.[44–46] In our investigated case, however, the low vibration frequency of the optical phonon modes causes their involvements in the low frequency thermal transport. Thus, all the XI_2 structures have comparable values of V_g for acoustic and optic phonon modes.

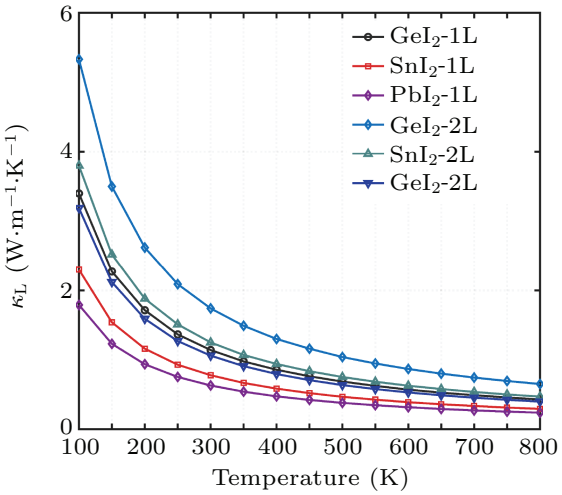


Fig. 3. Lattice thermal conductivity (κ_L) for XI_2 (X = Ge, Sn, Pb) monolayers and bilayers as a function of temperature (T) calculated using iterative solutions of the phonon Boltzmann transport equation.

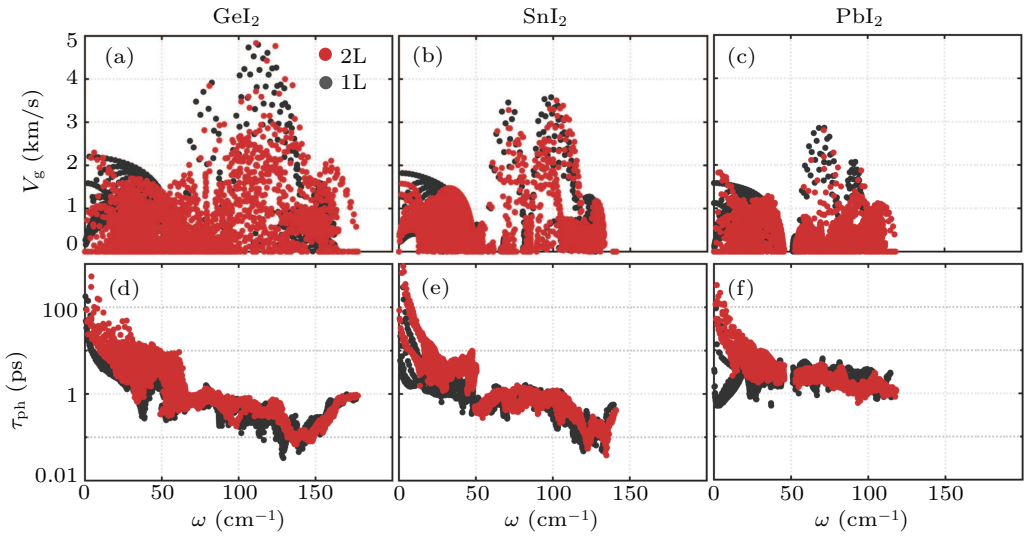


Fig. 4. Frequency-dependent phonon group velocity (V_g) (upper panel) and phonon lifetime (τ_{ph}) at 300 K (lower panel) for monolayers (black dots) and bilayers (red dots) of [(a), (d)] GeI_2, [(b), (e)] SnI_2, and [(c), (f)] PbI_2.

Phonon lifetime τ_{ph} is an important parameter to describe phonon anharmonicity according to Eqs. (2) and (3). It can be calculated by the reciprocal of anharmonic three-phonon scattering rates (ASRs)[47,48]

$$\frac{1}{\tau_{ph}} = \frac{1}{\tau_{anh}} + \frac{1}{\tau_{iso}}, \tag{5}$$

where $\tau_{ph}{}^{-1}$, $\tau_{anh}{}^{-1}$, and $\tau_{iso}{}^{-1}$ represent the total scattering rate (the inversion of total lifetime of phonons), the anharmonic scattering rate, and the isotopic scattering rate, respectively. Since the τ_{iso} is only related to the mass of element and has little effect on the scattering rate,[49] the value of τ_{ph} mainly depends on the anharmonic scattering rate. Our results of τ_{ph} for XI_2 monolayers and bilayers at 300 K are plotted in Figs. 4(d)–4(f). We find that for the low frequency modes, the phonon lifetimes are longer in the bilayers (red dots) than that in the monolayers (black dots), which may explain the larger κ_L of bilayer XI_2, as shown in Fig. 3.

Next, electronic structures for XI_2 monolayers and bilayers have been calculated. Our DFT–PBE results show that all the calculated structures are semiconductors and the monolayer band gaps are 2.09 eV, 2.03 eV, and 2.51 eV for GeI_2, SnI_2, and PbI_2, respectively, which are consistent with the previously reported values.[38] Given the heavy atomic mass of Sn, Pb, and I, we have taken the spin–orbital coupling (SOC) effect into consideration and present the DFT+SOC results of the band structures and DOS in Fig. 5. All the calculated structures have an indirect band gap with the value a little smaller than 2 eV. The band gap values of PbI_2 are smaller than the experimental results for the crystalline PbI_2 (2.346 eV at 300 K

to 2.487 eV at 20 K)[43] due to the well-known underestimation for semiconducting band gaps of the PBE functional. We thus checked the band gap values at the HSE06+SOC level of PbI_2. The obtained value of band gap for PbI_2 monolayer, bilayer, and bulk is 2.57 eV, 2.55 eV, and 2.49 eV, respectively. We find that the band gap for PbI_2 is not quite sensitive to the number of the layers and the value for the bulk is in good agreement with the experimental results at low temperature. The band gaps of the bilayers are slightly smaller than that of the monolayers in value, as the detailed values shown in Fig. 5. We find that for all the structures at the conduction band minimum (CBM) there is a fairly strong dispersion, which hints a high electron mobility, and consequently a high electrical conductivity when carrier concentration is large enough. We also note that for all the structures there are two energy peaks located between Γ–M and K–Γ in the valence band, whose energy differences are less than 0.1 eV. Such multiple degenerate valleys (separate pockets of Fermi surface with the same energy) at the valence band maximum (VBM) will help producing large Seebeck coefficient without causing the reduction of carrier mobility, which is beneficial to TE materials.[50–52] Considering values close to 2 eV of the band gaps, the optimal working temperature is around 2000 K according to the so-called "$E_g \sim 10k_BT_{opt}$" law,[53] but we here focus on the room temperature region.

To obtain the electron transport properties of XI_2, we calculated the carrier mobility of XI_2 by the deformation potential theory[54–57]

$$\mu = \frac{e\hbar^3 C_{2D}}{k_B T m^* m_d (E_1)^2}, \tag{6}$$

where C_{2D} is the elastic modulus for the 2D system, $m^* = \hbar^2 \left(d^2E/dk^2\right)^{-1}$ is the effective mass in the transport direction. We calculated m^* of an electron (hole) by fitting the band near the CBM (VBM) to a quadratic function. The average effective mass m_d can be calculated by $m_d = \sqrt{m^*_{\Gamma-M} m^*_{M-K}}$.[58] E_1 is the deformation potential defined by $E_1 = \Delta E_{edg}/(\Delta l/l_0)$, where ΔE_{edg} is the energy shift of the band edge with respect to the vacuum level under the applied uniaxial strain $\Delta l/l_0$. Then we calculated the relaxation time τ according to the following relation:

$$\mu = \frac{e\tau}{m^*}. \tag{7}$$

In Table 1 we list the calculated values of E_1, C_{2D}, m^*, μ, and τ at 300 K. We find a nearly isotropic behaviour in the electron mobility and relaxation time for both XI_2 monolayers and bilayers. In addition, the values of μ and τ for electrons in the bilayers are much larger than that in the monolayers, which indicates a dramatic enhancement of electron transport in the bilayers. In contrast, the μ and τ of the holes exhibit strong anisotropy in the monolayers but are much weaker in the bilayers. When compared with the monolayers, the τ for the holes in the bilayers are larger in the armchair direction but smaller in the zigzag direction.

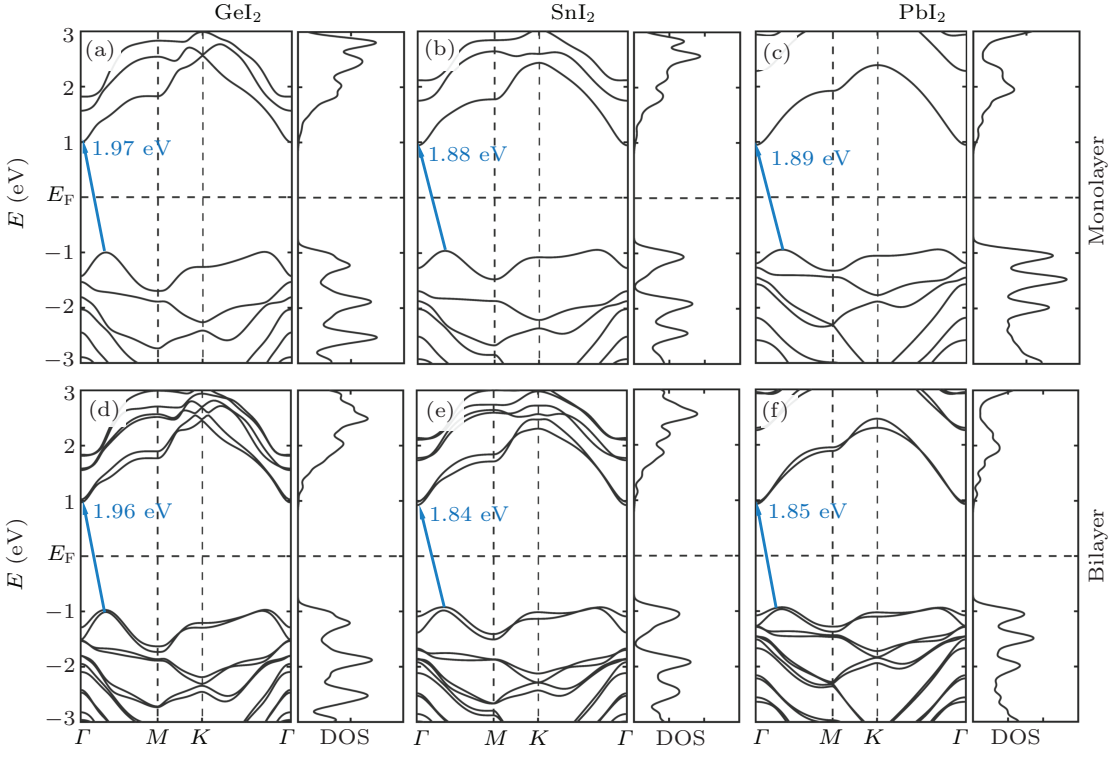


Fig. 5. Electronic band structure and density of states (DOS) for monolayers (upper panel) and bilayers (lower panel) of [(a), (c)] GeI_2, [(b), (e)] SnI_2, and [(c), (f)] PbI_2. The indirect band gaps are indicated by the blue arrows and the PBE+SOC values of band gaps are given.

Table 1. Deformation potential constant (E_1), 2D elastic constant (C_{2D}), effective mass (m^*), carrier mobility (μ), and relaxation time (τ) at 300 K for XI_2 (X = Ge, Sn, Pb) monolayers and bilayers. Calculated values for electrons and holes are denoted by 'e' and 'h'. Zigzag and armchair directions are denoted by 'zz' and 'ac'.

		Monolayer					Bilayer				
		E_1 (eV)	C_{2D} (N/m)	m^* (m_e)	μ ($cm^2 \cdot V^{-1} \cdot s^{-1}$)	τ (fs)	E_1 (eV)	C_{2D} (N/m)	m^* (m_e)	μ ($cm^2 \cdot V^{-1} \cdot s^{-1}$)	τ (fs)
GeI_2	e (zz)	5.51	23.71	0.23	308.64	40.36	5.50	48.10	0.22	686.18	85.83
	e (ac)	5.56	23.70	0.24	290.48	39.64	5.49	47.98	0.23	657.09	85.92
	h (zz)	2.74	23.71	0.71	68.32	27.58	3.62	48.10	1.02	27.71	16.07
	h (ac)	4.60	23.70	2.71	6.32	9.78	4.52	47.98	7.50	2.42	10.30
SnI_2	e (zz)	4.21	15.48	0.27	251.25	38.56	3.99	31.62	0.25	678.83	96.49
	e (ac)	4.20	15.51	0.28	243.42	38.75	4.00	31.56	0.25	674.88	95.92
	h (zz)	1.67	15.48	1.01	93.49	53.69	3.03	31.62	1.38	19.34	15.18
	h (ac)	4.10	15.51	1.56	9.99	8.86	3.06	31.59	5.50	4.75	14.87
PbI_2	e (zz)	3.35	13.93	0.33	236.35	44.34	3.28	28.57	0.29	689.62	113.70
	e (ac)	3.37	13.96	0.35	220.21	43.42	3.29	28.57	0.28	710.13	113.05
	h (zz)	1.32	13.93	1.19	63.56	43.00	2.81	28.57	2.42	12.91	17.77
	h (ac)	2.72	13.96	4.30	4.10	10.13	2.83	28.57	2.55	12.09	17.52

To further investigate the TE performance, in Fig. 6 we have plotted the S, σ, PF, and ZT as a function of carrier concentrations (n) (n-type for electrons and p-type for holes) for XI_2 monolayers and bilayers in both armchair and zigzag directions at 300 K. As shown in Figs. 6(a)–6(f), the S has negative values for n-type doping and positive values for p-type doping. For all the calculated structures, we find that the S displays no directional dependency and decreases with the increasing n. The p-type S is larger than n-type due to the degenerate valleys at the VBM. The values of S for the bilayers are larger than that of the monolayers.

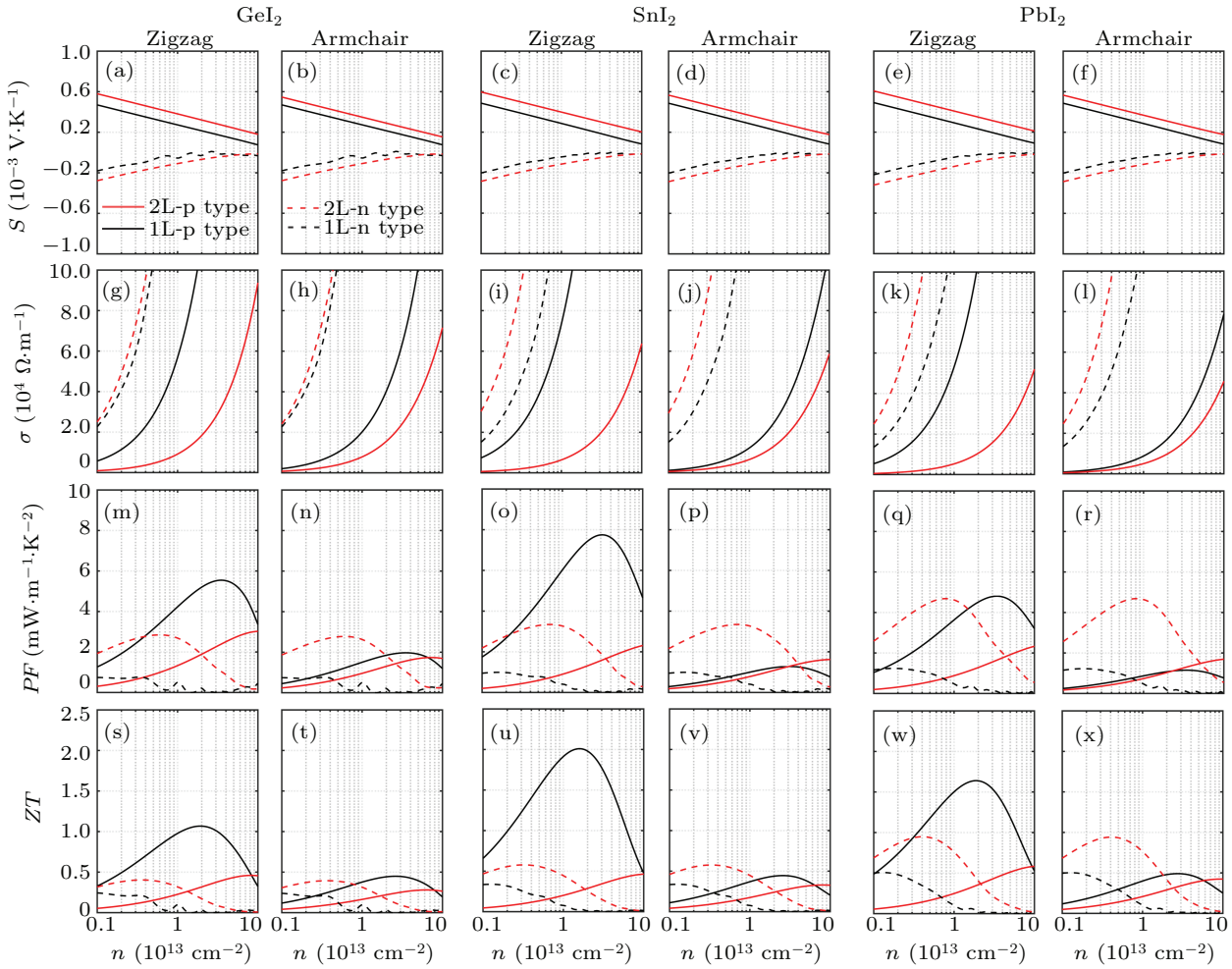


Fig. 6. Calculated [(a)–(f)] Seebeck coefficients (S), [(g)–(l)] electrical conductivity (σ), [(m)–(r)] power factor (PF), [(s)–(x)] figures of merit (ZT) as a function of the carrier concentration (n) for monolayers and bilayers of GeI_2 (left panel), SnI_2 (middle panel), and PbI_2 (right panel) at 300 K. The results along both zigzag (left sub-panel) and armchair (right sub-panel) directions are plotted. The p-type and n-type values are distinguished by solid and dashed lines. The results for monolayer and bilayer are distinguished by color.

From the σ plots depicted in Figs. 6(g)–6(l), we find that the n-type conductivity keeps isotropic and is greatly larger than the p-type conductivity. The p-type conductivity of monolayers shows significant anisotropy, while for the bilayers the anisotropy is much weaker. What is more, the n-type conductivity of XI_2 bilayers is larger than that of monolayers and for the p-type conductivity it is contrary. These results are consistent with the data of carrier mobility and relaxation time listed in Table 1.

The different behaviours of n- and p-type carriers mainly originate from the dramatic differences between the effective mass at the VBM of the monolayers and bilayers. As shown in Table 1, the values of m^* for the electrons in the bilayers are close to that in the monolayers. The μ and τ for the electrons in the bilayers are about twice as large as that in the monolayers due to their larger C_{2D}. However, the values of m^* for the holes are generally much larger in the bilayers, leading to the significantly lower μ and τ for the holes in the bilayers compared with the monolayers.

Incorporating all the physical quantities mentioned above, in the bottom two rows of Fig. 6 we have plotted the *PF* and *ZT* as a function of n. We find that the curves of *PF* and *ZT* have similar profiles. For the monolayers, both *PF* and *ZT* have much larger values for p-type doping than that for n-type doping. The maximum p-type *ZT* values reach 1.01 ($n = 2.10 \times 10^{13}$ cm^{-2}), 2.01 ($n = 1.69 \times 10^{13}$ cm^{-2}), and 1.64 ($n = 1.97 \times 10^{13}$ cm^{-2}) at 300 K along zigzag direction in GeI_2, SnI_2, and PbI_2 monolayers, respectively. The values of *PF* and *ZT* for p-type carriers in the bilayers (red lines) are lower than that in the monolayers (black lines). However, the n-type *PF* and *ZT* are greatly enhanced in the bilayers compared to the monolayers due to the larger Seebeck coefficient and electrical conductivity. The maximum n-type *ZT* values at 300 K for GeI_2, SnI_2, and PbI_2 bilayers reach respectively 0.40 ($n = 3.78 \times 10^{12}$ cm^{-2}), 0.58 ($n = 3.32 \times 10^{12}$ cm^{-2}), and 0.95 ($n = 4.23 \times 10^{12}$ cm^{-2}). In addition, the *PF* and *ZT* for the bilayers display much weaker in-plane anisotropy compared with the monolayers. The nearly isotropic *ZT* values provide consistent in-plane TE performance independent of direction for XI_2 bilayers.

Finally, the confinement effect of a 2D system has been considered. We calculated the *PF* enhancement factor (f_E), which is defined as $f_E = (L/\Lambda)^{D-3}$, where L is the spatial confinement length, $\Lambda = \sqrt{2\pi h^2/k_B T m^*}$ is the thermal de Broglie wavelength, and D is the dimensionality.[16,59] Here in our case of 2D XI_2, D is equal to 2. The values of Λ, L, and f_E for both the monolayers and bilayers are listed in Table A1 in Appendix A. We find that in all the structures the f_E for n-type doping is much larger than that for p-type doping, resulting from the significantly smaller effective mass at the CBM than that at the VBM, as shown in Fig. 5 and Table 1. The f_E values of $\sim$ 19–23 ($\sim$ 5–13) for n-type (p-type) doping in the monolayers and $\sim$ 10–12 ($\sim$ 2–6) for n-type (p-type) doping in the bilayers indicate the significantly enhanced TE performance of the 2D structures compared with their 3D counterparts.

4. Conclusion

In summary, by combining *ab initio* DFT calculations with the Boltzmann transport theory, we investigated the electrical and thermal transport properties and the TE performance of the XI_2 (X = Ge, Sn, Pb) monolayers and bilayers. Phonon spectra was calculated and the essentially absence of imaginary frequencies confirms the dynamical stability of all the 2D XI_2 structures. The relatively low frequency of the optical modes leads to their as significant contribution to the thermal conductivity as the acoustic modes, which is confirmed by the group velocity distribution. The values of the lattice thermal conductivity κ_L at 300 K for the bilayers are 1.74 W·m^{-1}·K^{-1}, 1.25 W·m^{-1}·K^{-1}, and 1.05 W·m^{-1}·K^{-1} for GeI_2, SnI_2, and PbI_2, respectively, which are about 1.6 times as large as that for the corresponding monolayers but still at a relatively low level. Electronic structure calculations show that all the monolayer and bilayer structures are semiconducting with an indirect band gap close to 2 eV and the bilayers have slightly smaller values of band gaps than the monolayers. In addition, the XI_2 bilayers have much higher electron mobility and relaxation time than the corresponding monolayers. The TE performance calculations show that the monolayers exhibit dramatically anisotropic TE performance and have higher efficiency for p-type doping than the bilayers. The highest p-type *ZT* values along zigzag direction reach 1.01, 2.01, and 1.64 at 300 K for GeI_2, SnI_2, and PbI_2 monolayers, respectively. The bilayers, however, exhibit nearly isotropic TE performance and have higher efficiency for n-type doping than the monolayers. The highest n-type *ZT* values reach 0.40, 0.58, and 0.95 at 300 K for GeI_2, SnI_2, and PbI_2 bilayers, respectively. The nearly isotropic *ZT* values provide consistent in-plane TE performance independent of direction for XI_2 bilayers.

Although the experimental results for the TE performance have not been reported so far, low thermal conductivity of PbI_2 has been experimentally measured[43] and 2D SnI_2 down to the monolayer has also been successfully prepared in experiment recently.[60] These encouraging experimental progresses supply a reasonable prospect of the applications for 2D XI_2 in TE materials. Our finding of the difference between the monolayer and bilayer for the doping type with superior figure of merit and the in-plane anisotropy indicates that the inter-layer interaction plays an important role in the TE performance of XI_2. It provides an effective tunability on the TE characteristics of few-layer XI_2 and will be of significant value in the relative experimental study in the future.

Appendix A: The confinement effect

Table A1. The *PF* enhancement factor (f_E) for XI_2 (X = Ge, Sn, Pb) monolayers and bilayers. L is the spatial confinement length and Λ is the thermal de Broglie wavelength. Calculated values in zigzag and armchair directions are denoted by 'zz' and 'ac'.

		Monolayer			Bilayer		
		Λ (nm)	L (nm)	f_E	Λ (nm)	L (nm)	f_E
GeI_2	n-type (zz)	17.94	0.775	23.15	18.35	1.550	11.84
	n-type (ac)	17.57		22.67	17.95		11.58
	p-type (zz)	10.21		13.17	8.52		5.50
	p-type (ac)	5.23		6.75	3.14		2.03
SnI_2	n-type (zz)	16.56	0.767	21.59	17.21	1.534	11.22
	n-type (ac)	16.27		21.21	17.21		11.22
	p-type (zz)	8.56		11.16	7.33		4.78
	p-type (ac)	6.89		8.93	3.67		2.39
PbI_2	n-type (zz)	14.98	0.786	19.06	15.98	1.572	10.15
	n-type (ac)	14.55		18.51	16.26		10.35
	p-type (zz)	7.89		10.04	5.53		3.52
	p-type (ac)	4.15		5.28	5.39		3.43

Acknowledgements

Project supported by the Fundamental Research Fund for the Central Universities and the Zhongying Young Scholar Program of Southeast University. We thank the Big Data Computing Center of Southeast University for providing facility support for performing calculations presented in this manuscript.

References

[1] Snyder G and Toberer E 2008 *Nat. Mater.* **7** 105
[2] Hicks L D and Dresselhaus M S 1993 *Phys. Rev. B* **47** 12727
[3] Hicks L D, Harman T C, Sun X and Dresselhaus M S 1996 *Phys. Rev. B* **53** R10493
[4] Lu P and Qu L 2013 *Chin. Phys. Lett.* **30** 017101
[5] Melnyk G, Bauer E, Rogl P, Skolozdra R and Seidl E 2000 *J. Alloys Compd.* **296** 235
[6] Zhu T, Liu Y, Fu C, Heremans J P, Snyder J G and Zhao X 2017 *Adv. Mater.* **29** 1605884
[7] Pei Y, Shi X, Lalonde A, Wang H, Chen L and Snyder G J 2011 *Nature* **473** 66
[8] Li G, Yao K and Gao G 2017 *Nanotechnology* **29** 015204
[9] Lv H Y, Lu W J, Shao D F, Lu H Y and Sun Y P 2016 *J. Mater. Chem. C* **4** 4538
[10] T Hung N, Nugraha A R T, Yang T, Zhang Z and Saito R 2019 *J. Appl. Phys.* **125** 082502
[11] Pei Y, Zheng L, Li W, Lin S, Chen Z, Wang Y, Xu X, Yu H, Chen Y and Ge B 2016 *Adv. Electron. Mater.* **2** 1600019
[12] Lin C, Lydia R, Yun J H, Lee H S and Rhyee J S 2017 *Chem. Mater.* **29** 5344
[13] Kim S I, Lee K H, Mun H A, Kim H S, Hwang S W, Roh J W, Yang D J, Shin W H, Li X S, Lee Y H, Snyder G J and Kim S W 2015 *Science* **348** 109
[14] Hicks L D and Dresselhaus M S 1993 *Phys. Rev. B* **47** 16631
[15] Hong J and Delaire O 1993 *Mater. Today Phys.* **10** 100093
[16] Dong B, Wang Z, Hung N T, Oganov A R, Yang T, Saito R and Zhang Z 2019 *Phys. Rev. Mater.* **3** 013405
[17] Li J, Zhang X, Chen Z, Lin S, Li W, Shen J, Witting I T, Faghaninia A, Chen Y, Jain A, Chen L, Snyder G J and Pei Y 2018 *Joule* **2** 976
[18] Wang Q, Quhe R, Guan Z, Wu L, Bi J, Guan P, Lei M and Lu P 2018 *RSC Adv.* **8** 21280
[19] Huang H H, Fan X, Singh D J and Zheng W T 2019 *J. Mater. Chem. C* **7** 10652
[20] Lv H Y, Lu W J, Shao D F and Sun Y P 2014 *Phys. Rev. B* **90** 085433
[21] Medrano Sandonas L, Teich D, Gutierrez R, Lorenz T, Pecchia A, Seifert G and Cuniberti G 2016 *J. Phys. Chem. C* **120** 18841
[22] Wickramaratne D, Zahid F and Lake R K 2014 *J. Appl. Phys.* **140** 124710
[23] Huang W, Da H and Liang G 2013 *J. Appl. Phys.* **113** 104304
[24] Guo H H, Yang T, Tao P and Zhang Z D 2014 *Chin. Phys. B* **23** 017201
[25] Peng B, Mei H, Zhang H, Shao H, Xu K, Ni G, Jin Q, Soukoulis C M and Zhu H 2019 *Inorg. Chem. Front.* **6** 920
[26] Hu Y F, Yang J, Yuan Y Q and Wang J W 2020 *Philos. Mag.* **100** 782
[27] Betal A, Bera J and Sahu S 2021 *Comput. Mater. Sci.* **186** 109977
[28] Shulenburger L, Baczewski A D, Zhu Z, Guan J and Tomanek D 2015 *Nano Lett.* **15** 8170
[29] Fugallo G, Lazzeri M, Paulatto L and Mauri F 2013 *Phys. Rev. B* **88** 045430
[30] Kresse G and Furthmüller J 1996 *Phys. Rev. B* **54** 11169
[31] Li W, Carrete J, Katcho N A and Mingo N 2014 *Comput. Phys. Commun.* **185** 1747
[32] Baroni S, Gironcoli S de, Corso A D and Giannozzi P 2001 *Rev. Mod. Phys.* **73** 515
[33] Togo A and Tanaka I 2015 *Scr. Mater.* **108** 1
[34] Madsen G K, Carrete J and Verstraete M J 2018 *Comput. Phys. Commun.* **231** 140
[35] Peng H, Kioussis N and Snyder J 2014 *Phys. Rev. B* **89** 195206
[36] Venkatasubramanian, R, Siivola E, Colpitts T and O'Quinn B 2001 *Nature* **413** 597
[37] Zhu Z, Cai X, Yi S, Chen J, Dai Y, Niu C, Guo Z, Xie M, Liu F, Cho J H, Jia Y and Zhang Z 2017 *Phys. Rev. Lett.* **119** 106101
[38] Naseri M, Hoat D M, Salehi K and Amirian S 2020 *J. Mol. Graph.* **95** 107501
[39] Zólyomi V, Drummond N D and Fal'ko V I 2014 *Phys. Rev. B* **89** 205416
[40] Zhang J, Xie Y, Hu Y and Shao H 2020 *Appl. Surf. Sci.* **532** 147387
[41] Ran R, Cheng C, Zeng Z Y, Chen X R and Chen Q F 2019 *Philos. Mag.* **99** 1277
[42] Cröll A, Tonn J, Post E, Böttner H and Danilewsky A N 2017 *J. Cryst. Growth* **466** 16
[43] Lin D, Guo B, Dai Z, Lin C and Hsu H 2019 *Crystals* **9** 589
[44] Zhang J, Liu H J, Cheng L, Wei J, Liang J H, Fan D D, Jiang P H and Shi J 2017 *Sci. Rep.* **7** 4623
[45] Peng B, Zhang H, Shao H, Xu Y, Ni G, Zhang R and Zhu H 2016 *Phys. Rev. B* **94** 245420
[46] Qin G, Yan Q B, Qin Z, Yue S Y, Hu M and Su G 2015 *Phys. Chem. Chem. Phys.* **17** 4854
[47] Peng B, Zhang H, Shao H, Xu Y, Zhang X and Zhu H 2016 *Sci. Rep.* **6** 20225
[48] Li W, Carrete J and Mingo N 2013 *Appl. Phys. Lett.* **103** 253103
[49] Klemens P G 1955 *Proc. Phys. Soc. A* **68** 1113
[50] Zhao Y, Dai, Z, Lian C, Zeng S, Li G, Ni J and Meng S 2017 *Phys. Rev. Mater.* **1** 065401
[51] Pei Y, Shi X, LaLonde A, Wang H, Chen L and Snyder G 2011 *Nature* **473** 66
[52] DiSalvo F J 1999 *Science* **285** 703
[53] Sofo J O and Mahan G D 1994 *Phys. Rev. B* **49** 4565
[54] Bardeen J and Shockley W 1950 *Phys. Rev.* **80** 72
[55] Mi X, Yu X, Yao K, Huang X, Yang N and Lü J 2015 *Nano Lett.* **15** 5229
[56] Ding Z, An M, Mo S, Yu X, Jin Z, Liao Y, Esfarjani K, Lü J, Shiomi J and Yang N 2019 *J. Mater. Chem. A* **7** 2114
[57] Bruzzone S and Fiori G 2011 *Appl. Phys. Lett.* **99** 222108
[58] Shafique A, Samad A and Shin Y H 2017 *Phys. Chem. Chem. Phys.* **19** 20677
[59] Hung N T, Hasdeo E H, Nugraha A R T, Dresselhaus M S and Saito R 2016 *Phys. Rev. Lett.* **117** 036602
[60] Yuan Q, Zheng F, Shi Z, Li Q, Lv Y, Chen Y, Zhang P and Li S 2021 *Adv. Sci.* **8** 2100009